Processability of high strength Aluminium-Copper alloys AW-2022 and 2024 by Laser Beam Melting in Powder Bed

M. Karg[1,2], B. Ahuja[1,2] , S. Kuryntsev[3], A. Gorunov[3] and M. Schmidt[1,2]

[1] Friedrich-Alexander-Universität Erlangen-Nürnberg (FAU), Department of Mechanical Engineering, Institute of Photonic Technologies, Konrad-Zuse-Str. 3-5, 91052 Erlangen, Germany
[2] Erlangen Graduate School in Advanced Optical Technologies (SAOT), Friedrich-Alexander-Universität Erlangen-Nürnberg, Paul-Gordan-Str. 6, 91052 Erlangen, Germany
[3] Department of Laser Technologies, Kazan National Research Technical University, K. Marx Str. 10, 420111, Kazan, Russia

```
REVIEWED
```

Abstract

Additive Manufacturing offers geometric freedom excellently suited for topology optimized light weight designs. Ideally these should be produced from materials of high strength to weight ratio such as aluminium-copper alloys. Yet these are considered unsuitable for welding. With Laser Beam Melting of Metals in powder bed (LBM), the only class of aluminium alloys widely processed is that of aluminium-silicon alloys, which are easily weldable and castable, too. In this contribution we present results of LBM high-strength aluminium-copper alloys AW-2022 and AW-2024 under variation of laser power, scan speed and hatch distance. We achieved relative densities well above 99 %. We analyzed thin walls, compared process windows as well as microstructures observed using etched metallographic microsections. We analyzed the chemical constitution of powders and produced samples using ICP-OES.

Introduction

The additive manufacturing technology of Laser Beam Melting in Powder Bed (LBM) is also known with slight variations under the registered trademarks of Selective Laser Melting™ SLM™, Direct Metal-Laser-Sintering® DMLS® or LaserCUSING™, each property of the respective owners. Industrial use of LBM has been increasing rapidly over the last years. Established fields of application include functional prototyping as well as small series production. Another field of LBM application with high economic viability is beginning to be commercially developed: the manufacture of light weight components, a famous example being the LBM injection nozzle by General Electric Company [17]. The layer-by-layer build-up inherent to LBM unlocks unmatched geometrical flexibility. This makes LBM especially suitable for realizing topology optimized designs with shapes that are optimized on a specific function or mechanical load case. Such designs typically include undercuts and can often only be manufactured conventionally after severe adaptations. Compromising optimal geometry to comply with the restrictions of production technologies reduces the added value in weight savings. The geometric flexibility of LBM can also be used to produce integral designs which would otherwise have to be assembled from multiple parts. All joining seams are zones of potential mechanical weakness and therefore safety factors must be used. Hence, total weight

420

increases. Integral designs also save weight by eliminating the need for special geometry elements for joining, such as flanges.

Light weight by design can be complemented by light-weight materials. Those need to reach the mechanical properties required with a minimum of weight. For structural mechanical applications, high tensile strength and elongation at break are examples of such desirable properties. High-strength age-hardenable aluminium-copper alloys form a class of engineering materials which has been continuously popular for light-weight applications ever since their discovery in 1901 [19]. However, to the knowledge of the authors those alloys have not been researched for use in LBM, yet. This can be explained by the common rating of such alloys as being unweldable and LBM physically being a welding process. Instead, almost exclusively aluminium-silicon alloys are popular in LBM research and industrial use. They have significantly lower strength-to-weight ratios than aluminium-copper alloys [1]. The most widely spread aluminium alloy in LBM is AlSi10Mg.

The risk of failure to create dense samples from age-hardenable aluminium-copper alloys must be considered very high. On the other hand the potential benefit for LBM in case of success is also very high. Because no reference exists in LBM of aluminium-copper alloys, two different alloys are experimentally compared over a wide range of LBM process parameters. The goal of this research is to investigate the suitability of the two exemplary aluminium-copper alloys AW-2022 and 2024 to produce dense parts by LBM.

Materials and Methods

Metal Powders

Representing the established state of the art in LBM, the cast alloy EN AC-43000. The designation AC stands for "Aluminium Cast". AC-43000, also known as AlSi10Mg, has been processed as a point of reference [1]. After LBM manufacture and subsequent T6 heat treatment (that is solution annealing and artificial aging) AlSi10Mg typically reaches an ultimate tensile strength around 300 MPa, an elongation at break of 5-10% and a mass density of 2,64 g/cm³. Being close to the Al-Si eutectic, this alloy exhibits a melting point at about 570 °C which makes it well suited for crack free casting and welding.

For this research, we chose the two aluminium-copper alloys AW-2022, which is also known as AlCu5Mg0.5, and AW-2024, also known as AlCu4Mg1. Both alloys are classified as wrought alloys with the designation AW. Processing through the liquid phase is to be avoided in favor of forming processes or joining by rivets. They are considered to be weldable only under difficulties, via friction welding or with aluminium-silicon filler material. AW-2024 is one of the most widely used aluminium-Copper alloys for structural applications, e. g. in aircraft bodies. The reasons are its high tensile strength of over 480 MPa, an elongation at break of 18 %, a fatigue strength of 138 MPa and a mass density of 2,78 g/cm³ when conventionally manufactured and T3 heat treated (that is solution annealed, cold forged and aged) [18]. Compared to LBM-AlSi10Mg, conventionally manufactured AW-2024 offers a 60 % increase in ultimate tensile strength, about two and half times the elongation at break but only a 5 % increase in mass density. Thus, it is far more attractive for light weight design.

For AW-2024, the solidification interval measures 136 K [2]. AW-2022 has a similar chemical constitution and thus a similar interval between liquidus and solidus temperatures is expected as with AW-2024. The width of the solidification interval is related to the susceptibility

Table 1: Chemical composition of investigated alloys in weight percent, single numbers indicate maximum contents. Key constituents for crack susceptibility are colored [5, 6, 7, 8]

EN	Chem.	Si	Fe	Cu	Mn	Mg	Cr	Zn	Ti	Ni	Sn	Pb	Al
AW-2022	AlCu5Mg	0.15	0.2	4.5-5.5	0.15-0.5	0.1-0.45	0.05	0.05-0.3	0.15	-	-	-	balance
AW-2024	AlCu4Mg1	0.5	0.5	3.8-4.9	0.3-0.9	1.2-1.8	0.1	0.25	0.15	-	-	-	balance
AC-43000	AlSi10Mg	9.0-11.0	0.55	0.05	0.45	0.2-0.45	-	0.1	0.15	0.05	0.05	0.05	balance

for hot cracking, which is a major issue in welding of Al-Cu wrought alloys [3, 4]. The chemical compositions of the three alloys investigated are shown in Table 1.

Most obvious differences in chemical composition are the percentages of the main alloying elements Silicon and Copper, respectively. Furthermore, in AC-43000, higher contents of impurity elements are tolerated. That is, because AC-43000 is typically produced from recycled aluminium scrap as a secondary alloy, whereas AW-2022 and AW-2024 are primary alloys created directly from ore. Outside Additive Manufacturing, AC-43000 is not only common as an alloy for sand or die casting but also as a filler material for welding under the designation of S Al 4046 [9, 10, 11]. Al-Si based fillers are particularly useful for joining parts made of Al-Cu alloys, which are difficult to weld successfully at all [12, 13, 14]. The lower strength of a weld seam with Al-Si filler compared to base materials made of high-strength Al-Cu joining partners can be compensated by means of design, e. g. a larger cross section area of the weld seam. For LBM, this is obviously not an option, because here parts are built up from weld seams only and there are no semi-finished products being joined.

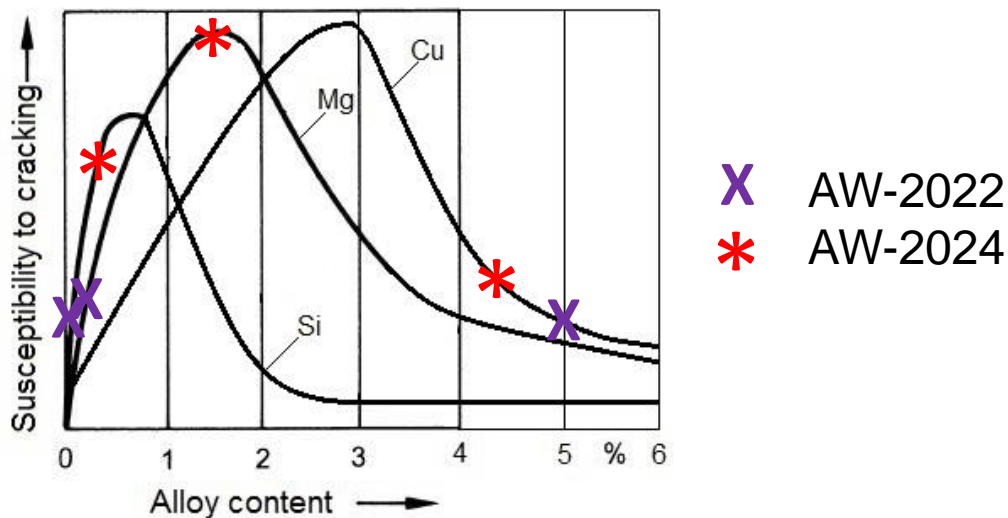According to [4], copper content between 0.33 and 5 weight-percent results in increased

Fig. 1 Weld crack susceptibility of aluminium alloys depending on Silicon, Copper and Magnesium contents. Contents of AW-2022 and AW-2024 highlighted [16]

susceptibility of aluminium alloys to hot cracks in welding. Magnesium content between 1 and 2 %, as it can be found in AW-2024, but not in AW-2022, is considered to be most unsuitable for crack-free welding [15]. Even silicon can increase the tendency towards cracking, if the alloy content is below 2 % [16]. The correlations between contents of Mg, Si and Cu in aluminium alloys and susceptibility to weld cracking are illustrated in Fig. 1. The percentages of these elements in AW-2024 are all in regions known to facilitate crack formation more strongly than in AW-2022. Considering the similarities between classic welding and LBM, the hypothesis can be formulated that AW-2022 should be better suited for LBM than AW-2024. Nevertheless, the general expectation is that successful production of samples with high relative density by LBM with these wrought alloys is very difficult. Analyzing two slightly different alloys in comparison might help to better understand the influencing factors on suitability for LBM.

However, the mechanisms behind hot-cracking are complex and not entirely understood, yet [15]. Also factors other than crack susceptibility might influence the LBM processability. Compared to conventional welding, LBM is characterized by smaller melt pools, higher feed rates and faster cooling rates.

Successful laser beam welding of the similar alloy AW-2017A (AlCuMg1) has been performed in research using pulsed Nd:YAG lasers [3]. In contrast, industrialized LBM is based on Yb:YAG fiber lasers with higher beam quality in continuous wave mode to ensure both high detail resolution and agreeable productivity.

The wrought aluminium alloy powders for the research presented in this contribution, AW-2022 and AW-2024, have been sourced from supplier TLS Technik GmbH. TLS had atomized both under an argon atmosphere. The cast alloy AC-43000 had been atomized under nitrogen atmosphere by supplier Ecka Granules Germany GmbH. All powders are prealloyed. We have sieved all powders with a vibration sieving device under argon atmosphere between meshwidths of 20 µm and 63 µm. In order to avoid cross-contamination, we have cleaned the sieves in a water-detergent solution and dried them using a hot air stream before sieving another powder.

Experimental procedure - Laser Beam Melting

We use an SLM 50 LBM machine of ReaLizer GmbH. It features a rotational recoater with a flexible silicone rubber lip in contact with the powder and a single-mode Yb:YAG fiber laser with a wavelength of 1070 nm and a maximum output power of 100 W. The manufacturer specifies a minimum focus diameter of 10 µm. We have blasted the aluminium build platforms with corundum (Al_2O_3) particles driven by pressurized air to ensure homogeneous powder coating and sufficient connection of the first molten layer. The process chamber is flushed with argon. We use a constant pre-heating temperature of 200 °C. We keep the layer thickness constant at 30 µm. We vary laser power, hatch distance and scan speed. For the production of cubic samples with an edge length of 5 mm, the scan direction is alternated by 90 degrees from layer to layer. We do not use stripes or chess-board patterns, because the scan vectors' length is limited by the small sample size.

Machine-manufacturer-specific scan mirror control requires indirect setting of scan speed through two separate values: point distance and exposure time. For a wide range of combinations, we had previously measured the resulting scan speeds of the laser spot in the powder bed with a

significance, only the mean values of the measured scan speeds are given in this contribution instead of the settings for point distance and exposure time. Each mean value has been calculated from seven measurements.

We approach the manufacturing process of LBM step by step with increasing complexity as shown in Fig. 2. We produce and analyze firstly single melt tracks on the build platform, secondly thin walls built from vertically overlapping single melt tracks, thirdly cubes on the platform and finally cubes on support structures. In industrial use, LBM parts will be built on supports, if the platform is not supposed to be joined and form an element of the product, like it is frequently the case e. g. in tooling applications. Thermodynamic situations are expected to be different from cubes directly on the platform considering the low thermal conductivity of loose powder and the comparatively small cross sections of the supports. Unlike e. g. in Electron Beam Melting, loose powder in LBM is neither molten nor sintered. Heat transport mechanisms during solidification might have considerable influence on the LBM processing of alloys sensitive to welding conditions such as the ones investigated. We have not used contour scanning and made no effort to optimize surface roughness, as it is of secondary interest compared to the goal of high relative density. We estimate suitable hatch distances for cubic volume samples based on the width of thin walls. We expect that combinations of laser power and scan speed which prove in thin walls perform well in cubes, too. Additionally, the results from thin walls can be directly applied as parameters for filigree supports designed by the industry-standard software tool Magics Support Generation, which is used as build 17.1.1.2.
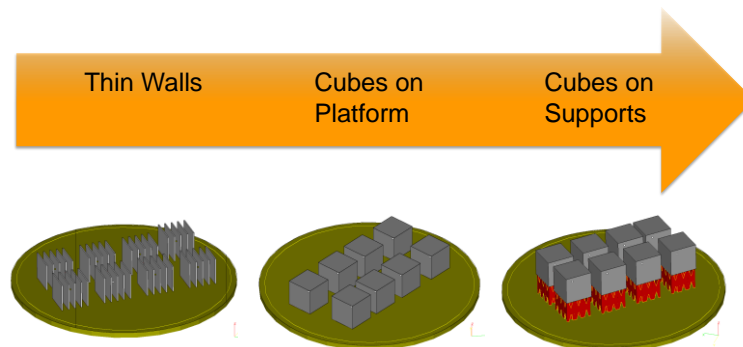

Fig. 2 The gradual approach used to assess a material's suitability for LBM

Analysis

For metallographic preparation, we cut platforms in handy pieces, embed them in epoxy resin, grind and polish with subsequently finer grain. We determine relative density by image analysis of reflected light micrographs obtained from polished microsections. We combine several microscope images by stitching, convert first to greyscale, then to black and white based on a threshold value and define a region of interest excluding the rough outer surface of samples. Then black and white pixels are counted by the freeware image analysis tool GIMP 2.8 to calculate the relative density. All metallographic sections shown in this paper are oriented parallel to the build-up direction. For microstructure analysis, we etch samples using Bohner's reagant. Chemical Analysis is performed at Institute of Particle Technology (LFG) by Jochen Schmidt with the method of inductively coupled optical emission spectroscopy (ICP-OES) using an Optima 8300 device from Perkin Elmer.

Results and Discussion

Powder Characterization

As shown in Fig. 3, the particle shapes are round without sharp edges, however not perfectly spherical. Especially the nitrogen-atomized particles from AC-43000 appear more irregular, rather potato-like in shape. The particle surface appears to be not perfectly smooth, yet not fissured as e. g. is common for powders atomized with air or water. In spite of repeated sieving, all powders do still include particles smaller than 20 μm.
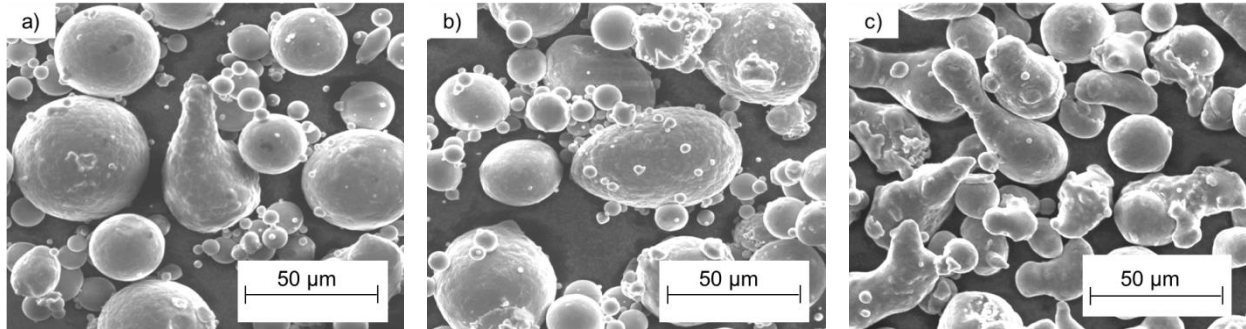

Fig. 3 SEM pictures of sieved powders, a) AW-2022, b) AW-2024 c) AC-43000

When prepared as metallographic microsections, all of the three powders exhibit porous particles, as shown in Fig. 4. This is typical for inert gas atomized powders. The percentage of porous particles is low, as illustrated in Fig. 5. A quantitative statement cannot be made based on the relatively small number of sectioned particles. Unlike in solid-state sintering, no proof exists that powder porosity persists through full melting in LBM and causes part porosity. In the LBM machine, all three powders result in reliably homogeneous powder layers as far as it can be judged with the naked eye.
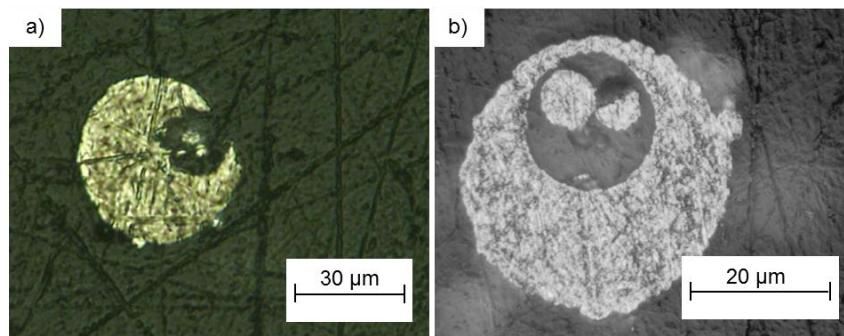

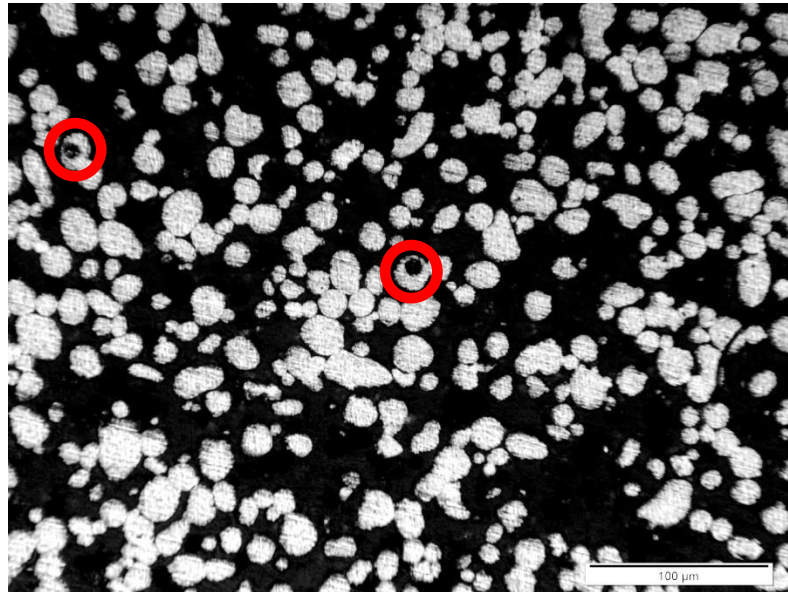Fig. 4 Metallographical microsections of powders a) AW-2022, b) AW-2024

425

Fig. 5 Reflected-light microscope picture of microsection of powder AC-43000, highlighted in red circles: porous particles

Single Melt Tracks

We create single melt tracks of 5 mm length on the substrate platforms using 12 different scan speeds between 20 and 500 mm/s, combining each scan speed with a laser power from 70 W to 100 W in steps of 5 W. We perform this using the two wrought aluminium alloys and analyze the results using reflected light microscopy. Tendencies can be guessed: laser powers above 90 W and scan speeds between 44.9 mm/s and 250 mm/s seem to be better suited than other parameter combinations because they result in more homogeneous melt tracks. However, the results do neither show consistency nor reproducibility. We attribute this to relatively large variations of the first powder layer on the platform due to the flexible silicone-rubber lip of the recoater on the machine used.

Thin Vertical Walls

Compared to single melt tracks, thin walls inherently contain a better statistic averaging of variations in powder layer thickness. Thus they allow stronger statements about the processability of a certain powder. We use the same parameter combinations as for single tracks and add the scan speeds of 746.9 mm/s and 1047.4 mm/s for AW-2022. After the LBM process and subsequent removal of loose powder, it can be seen that all parameter combinations result in walls that are standing solidly on the platforms. Exemplary samples of microsections created from thin walls of AW-2022 and AW-2024 are compared in Table 2. The effect of the scan speed on the width and homogeneity of the walls is obvious: with 44.9 mm/s, the walls are of irregular shape, characterized by appendages. These appendages are much larger than the powder particles, so they must have formed from melt. This explanation fits their teardrop shape, which appears to be hanging downwards in the direction of gravity and towards potential capillary forces exerted from the powder bed. With increasing scan speeds, the appendages become smaller and fewer.

Table 2: Reflected light microscopy of thin walls with 1 mm distance, embedded in transparent resin, grinded and polished, left: AW-2022, right AW-2024
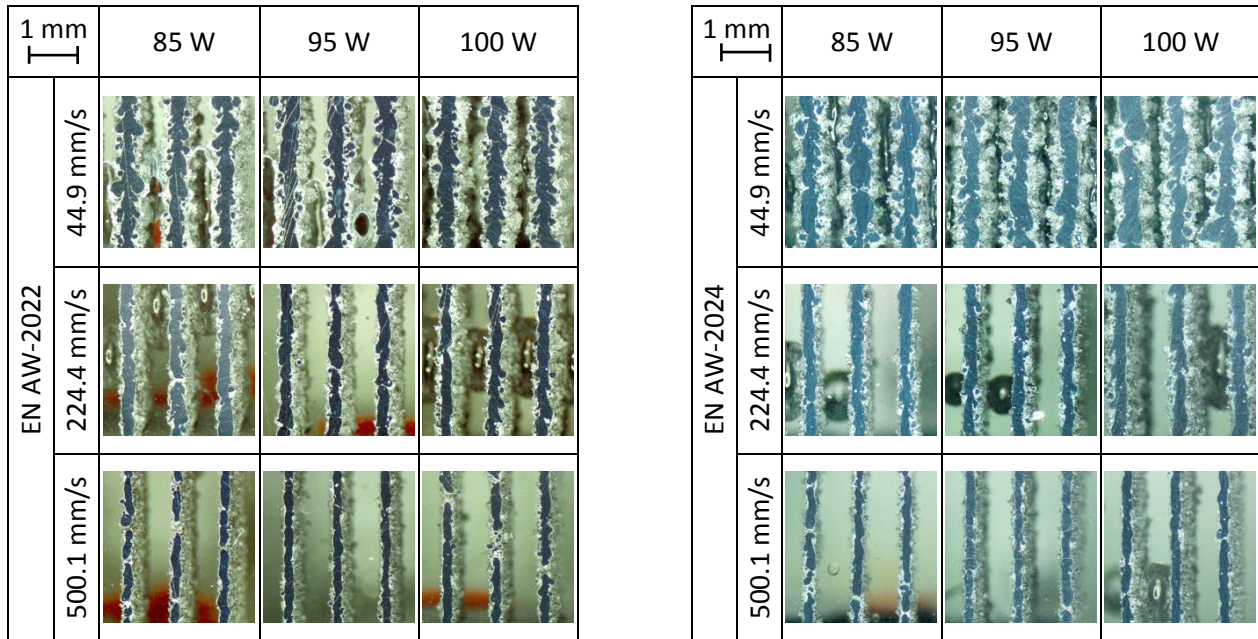
The obvious interpretation is that faster scanning leads to less energy input per length, which causes smaller melt pools and faster solidification, so that no drop-shaped appendages can form. The width of the walls is reduced with higher scan speeds. No significant differences can be found between the two wrought alloys. However, we suspect a slight shift of AW-2024 towards higher scan speeds. As expected, the 18 % increase in laser power from 85 W to 100 W has less obvious effects on the thin walls compared to the 1014 % increase of the scan speed from 44.9 mm/s to 500 mm/s. With AW-2022, thin walls have also been produced with scan speeds of 746.9 mm/s and 1047.4 mm/s, the microsections are shown in Table 3. These higher scan speeds have resulted in walls with more numerous defects. At 1047.4 mm/s, the influence of laser power becomes prominent: thin walls show less defects with 100 W than with 85 W. As a reference point, on the right of Table 3, two exemplary microsections of thin walls from AC-4300 are shown which were produced with scan speeds of 157.4 mm/s and 900 mm/s. Unlike with the wrought alloys, no melt drop appendages can be seen at low scan speed. Defects are much less frequent than with the wrought alloys. The width of thin walls made from AC-43000 consistently decreases with increasing scan speed.

This can in general be explained by the increasing amount of energy deposited with lower scan speeds and with the less rapid cooling and solidification. The lack of drop-shaped appendages with AC-43000 might be due to its abrupt solidification when the melting point of 570 °C is reached. The aluminium-copper alloys have a wide melting range, with the solidus temperature of AW-2024 at 502 °C being lower than the melting point of AC-43000. The large mushy zone between solidus and liquidus might effectively lead to a longer lifetime of the melt at low scan speeds. During this time, the drop-shaped appendages might form, driven by gravity or capillary forces. The increasing occurrence of defects at high scan speeds compared to AC-43000 might be caused by worse wetting of the molten aluminium-copper alloys. This might be influenced by viscosity and surface tension.

Table 3: Reflected light microscopy of thin walls with 1 mm distance, embedded and polished, left AW-2022 with higher scan speeds, right EN-AC 43000 with wider range of speeds
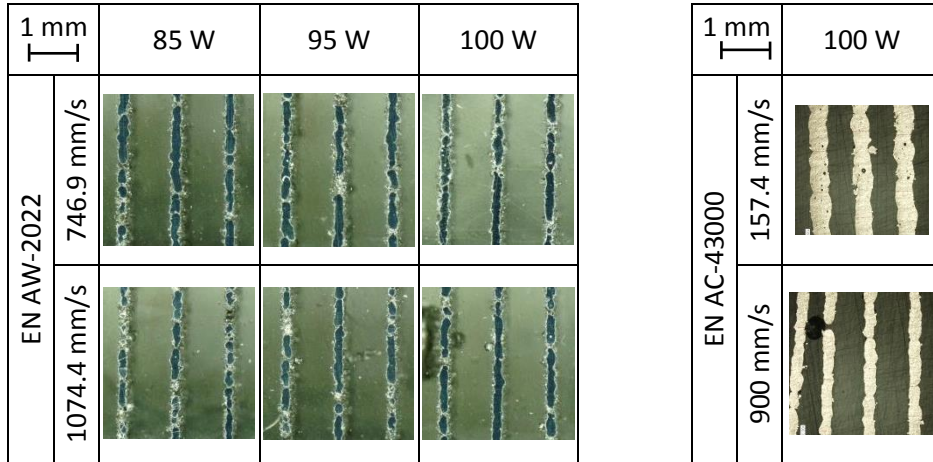
Cubes on platform

Cubes on platforms are produced from both wrought alloys. The laser power is kept constant at 100 W based on the results from thin walls. With 2022, we used scan speeds between 63.5 mm/s and 343.5 mm/s and the two hatch distances $d_{Hatch} = 80$ µm and $d_{Hatch} = 100$ µm. Fig. 6 shows the resulting relative densities of the sample cubes without supports. The highest relative densities above 97 % are achieved within a range of scan speeds between 175 mm/s and 265 mm/s. This is roughly the same range that resulted in homogeneous thin walls of AW-2022. With these results, no clear statement can be made about the effect of the two hatch distances. With AW-2024, we used scan speeds between 63,5 mm/s and 343.5 mm/s and the two hatch distances $d_{Hatch} = 60$ µm and $d_{Hatch} = 100$ µm. With AW-2024, the highest relative densities of $\rho_{rel} = 98.3$ % are achieved with $d_{Hatch} = 100$ µm. With AW-2022, only 97.3 % are reached. Fig. 7 shows the cross sections of the samples with the lowest porosity for each material. Significantly higher scan speeds with AW-2024 compared to AW-2022 are observed.
A possible explanation could be that AW-2024 might have a wider solidification interval
between solidus and liquidus and benefit from faster cooling, which is a result of faster scanning.
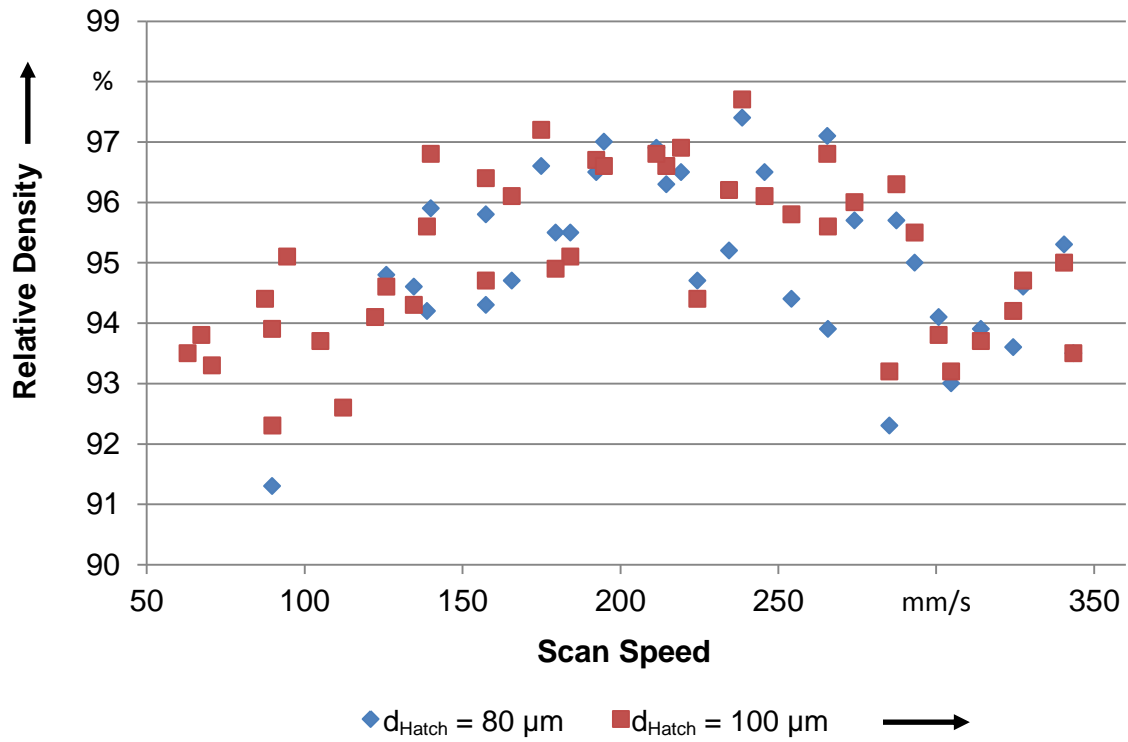
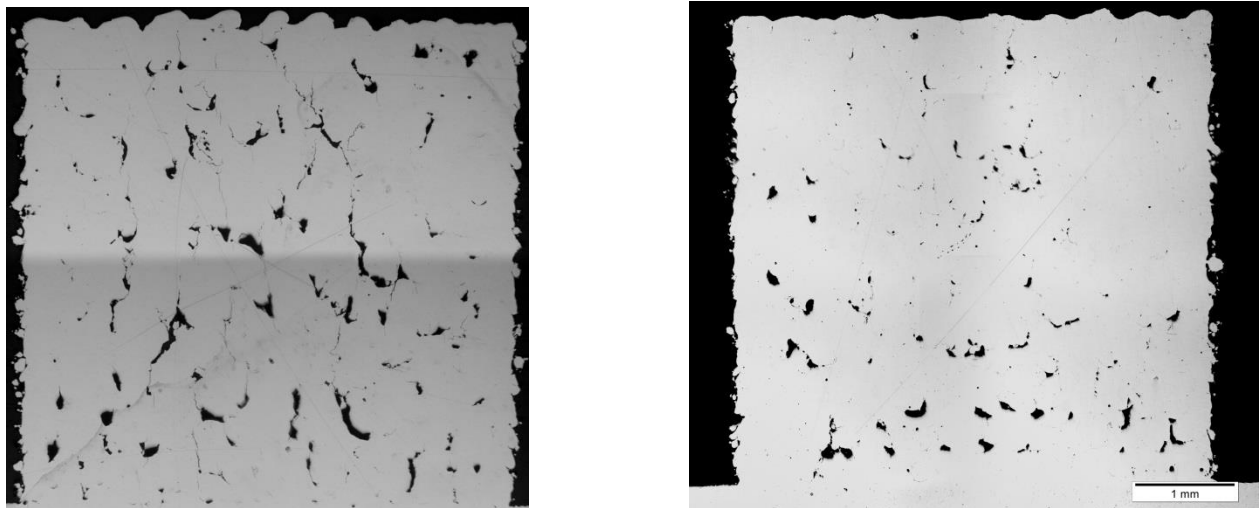Fig. 6 Relative density of AW-2022 cubes on platform over scan speed

Fig. 7 Cubes on platform, left AW-2022, ρ_{rel} = 97.3 %, 100 W, 167.4 mm/s, d_{hatch} = 110 μm; right AW-2024, ρ_{rel} = 98.3 %, 100 W, 245.7 mm/s, d_{hatch} = 100 μm

Cubes on Support

For building cubes on support, the laser power is again kept constant at 100 W. Hatch distances of 30 µm, 70 µm, 110 µm and 150 µm are used, the scan speed is varied between 100 mm/s and 300 mm/s.

The results for AW-2022 are shown in Fig. 8. The highest relative densities above 99.5 % are achieved in a range of scan speeds between 195 mm/s and 245 mm/s for a hatch distance of 70 µm. They follow a consistent trend with few outliers. The hatch distance of 110 µm is not suitable for such high relative densities, 150 µm results in even lower percentages. With 30 µm, some samples show very high relative densities, but large variations indicate a less robust process with low reproducibility. The best results are achieved within a sub-range of the scan speeds that lead to homogeneous thin walls or highly dense cubes on the platform, respectively. Higher relative densities are achieved on supports compared to cubes with contact to the build platform on their full cross section.

With AW-2024, $d_{Hatch} = 150$ µm is not considered because no high relative densities are to be expected. The results for AW-2024 are shown in Fig. 9. Relative densities above 99.75 % are achieved for scan speeds between 150 mm/s and 300 mm/s, which is a considerably wider process window compared to AW-2022. Between 265 mm/s and 295 mm/s, even relative densities above 99.9 % are achieved. As with AW-2022, the best results are achieved in a sub-range of the scan speeds which lead to homogeneous thin walls. For AW-2024, homogeneous thin walls could be produced between 150 and 500 mm/s. However, unlike with AW-2022, there seems to be an unexpected correlation of relative density and hatch distance if the results are
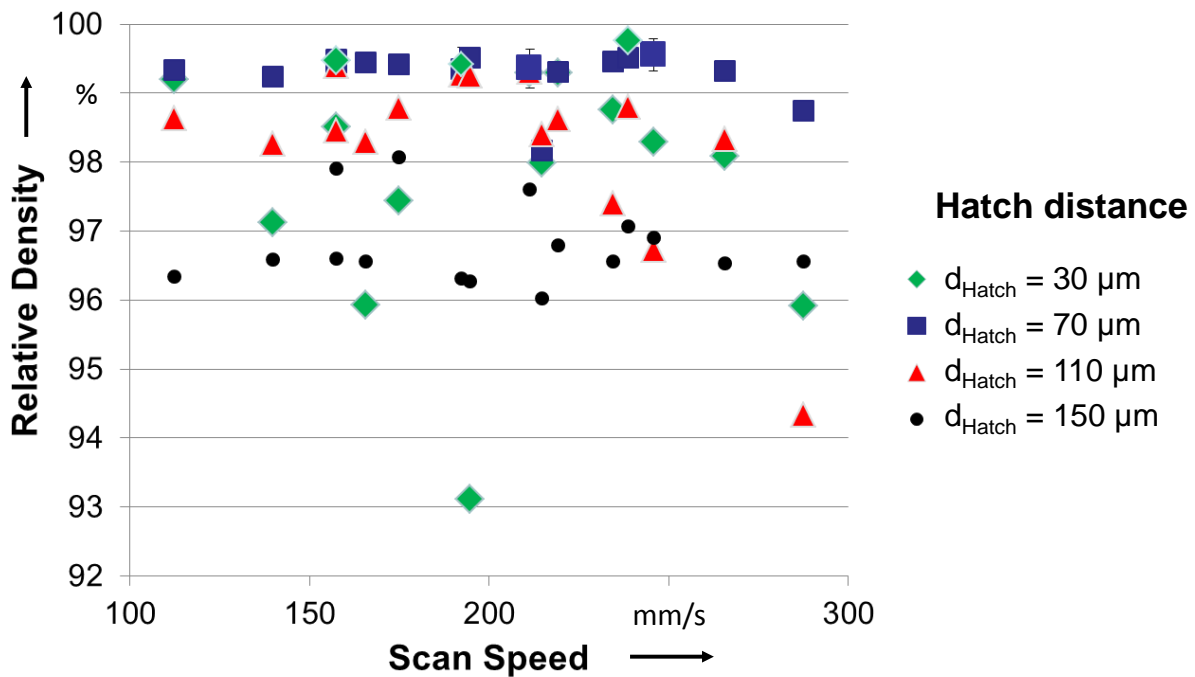
Fig. 8 AW-2022 cubes on supports, relative density over scan speed. Values including standard deviations were obtained from 3 microsections of each cube

compared to cubes without supports. The cubes on supports built from 2024 achieve the highest relative densities for $d_{Hatch} = 30$ μm, which was not the case for cubes without supports. Most obvious difference between these experiments is the heat conduction away from the melt pool through the platform towards the machine bed. It should be much faster for the cubes without supports. The cross section area of supports is rather small compared to a full face of a cube and the loose powder acts as a thermal insulator.
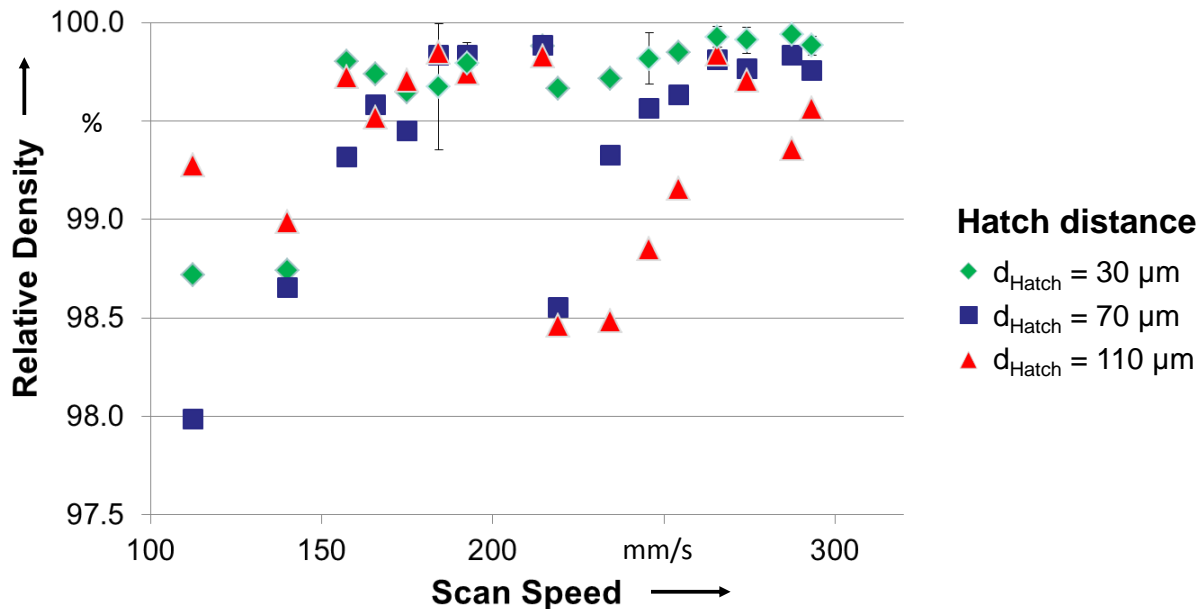

Fig. 9 AW-2024 cubes on supports, relative density over scan speed. Values including standard deviations were obtained from 3 microsections of each cube

In comparison to AW-2022 the highest relative density of cubes on supports made of AW-2024 are produced at significantly higher scan speeds and smaller hatch distance. The range of scan speeds is wider for AW-2024 as well as the absolute values of maximum relative densities. This can be an indication of lower sensitivity against variations of the process conditions which might lead to a more robust LBM process. As all other conditions such as powder particle size, atomization procedure or LBM machine used have been identical, the reasons should be in the different chemical composition of the alloys. AW-2024 contains significantly higher amounts of magnesium and silicon compared to AW-2022. A magnesium content like in AW-2024 is considered a disadvantage for crack-free welding. Due to the focus of our analysis on relative density, cracks might be neglected though, as they have little cross section area and thus little effect on relative density. They should be all the more noticeable in the results of tensile tests, however. Silicon is usually understood to reduce melt viscosity of aluminium alloys and to have beneficial effects on coalescence. Voids with incomplete

However, all experiments presented in this paper have been conducted with samples of small dimensions on a specific machine with a maximum laser power of 100 W. Real production parts made out of aluminium would typically have larger dimensions and more complex geometries. Under such circumstances, results might vary locally. Absolutely higher residual stresses as well as larger variations in thermodynamic conditions and hence more issues with hot and cold cracks could be consequences. On the other hand, higher laser powers, as common in LBM machines with larger build envelopes, might enable more robust parameter sets.

As the most frequent starting points for cracks in the cubic samples the bottom surface of cubes has been identified. Examples are shown in Fig. 10.

Fig. 10 Etched microsections of cubes on supports, left AW-2022, right AW-2024

These cracks appear to begin at irregularities of the first fully exposed layers above the supports. They propagate through multiple layers. Strategies to reduce such cracks may be optimization of the exposure parameters for the first layers with loose powder underneath and the adaptation of support geometries.

The etching uncovers the typical pattern for LBM parts created with 90° alternating scan direction from layer to layer, as shown in Fig. 8. With AW-2024, epitaxial columnar grain growth becomes more prominent towards center and top of the sample, rough boundaries indicated with dotted lines. This is also typical for additive manufacturing processes with the main temperature gradient in direction of the build-up.

Chemical Analysis

Chemical Analysis of both wrought alloy powders has been performed by inductively coupled plasma optical emission spectroscopy (ICP-OES). The results are shown in Fig. 11. In the AW-2022 powder, a magnesium content of only 0.082 wt.-% is measured with a standard
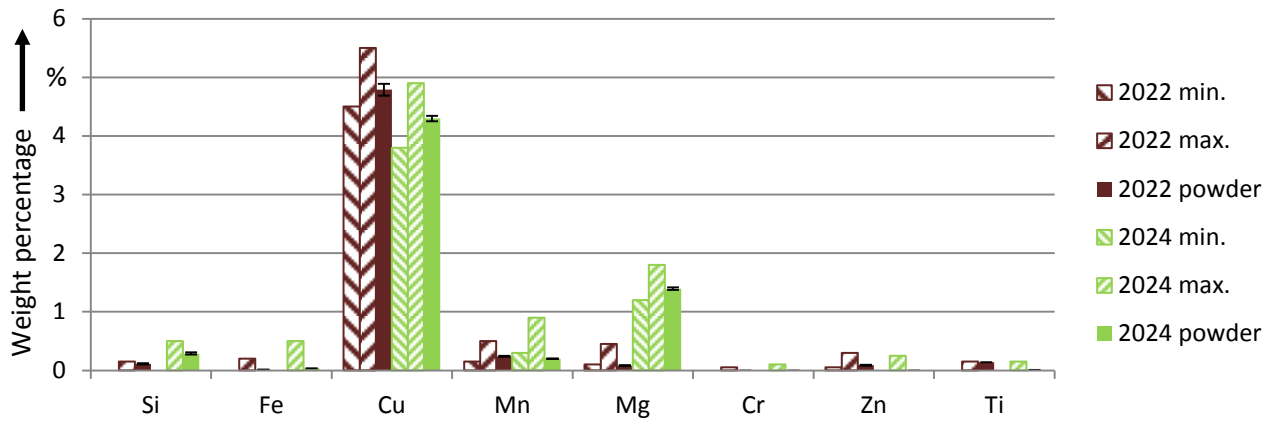
432

Fig. 11 Content of chemical elements in the used powders compared to upper and lower limit of respective alloy standard

deviation of 0.009 wt.-%, while the standard requires 0.1-0.45 wt.-%. In the AW-2024, a manganese content of 0.199 wt-% is measured with a standard deviation of 0.005 wt.-%, the standard requires 0.3-0.9 wt.-%. All other elemental percentages are within the limits for the respective alloy.

The cube on support sample of AW-2024 with the highest relative density has also been measured and compared to the powder as well as to the percentages in the definition of the alloy – as mentioned above in Table 1. The results of this comparison are shown in Fig. 10. ICP-OES measurements are given as a percentage of the maximum content according to the alloy definition. If the standard contains a minimum value, this is represented in the blue bars. If there is no blue bar present, the minimum allowed percentage of the respective element is 0. The contents of Nickel, Tin and Chromium were below the detection limits. Chromium and Zink are allowed a maximum value in AW-2024, so they are still represented in Fig. 12. After LBM, all elements are within the range allowed for AW-2024. However, many of them increase their content, but some remain unchanged within the standard deviation represented as black I-shaped error bars in the diagram. A possible explanation is that aluminium evaporates preferredly during LBM.
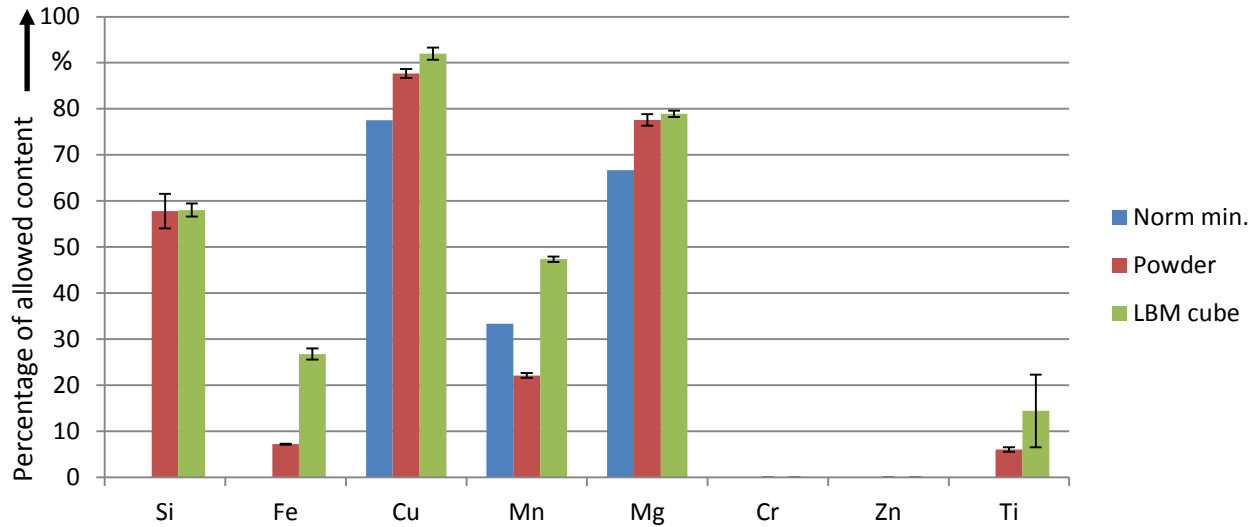
Fig. 12 AW-2024: content of chemical elements in percent of maximum value according to alloy standard, before and after Laser Beam Melting

Summary and Outlook

We showed that wrought aluminium alloys AW-2022 and 2024 can be processed to high relative densities above 99.5 % relative density by LBM. This is not self-evident, because they are not considered to be easily processed through the liquid phase, hence their classification as wrought alloys. Alloy 2024 exhibited a slightly larger parameter window and higher absolute values of relative density. We assume this to be caused by the higher content of silicon compared to 2022. We confirmed the processed powders to be in fact representative for the non-atomized alloys' composition by inductively coupled optical emission spectroscopy. Analysis of chemical constitution of AW-2024 in powder form and after LBM also indicated that aluminium evaporates preferredly, raising the contents of most other constituents, but without exceeding the boundaries for definition of the alloy.

We used a step-wise experimental approach by consecutively building up single melt tracks, thin walls, cubes on the platform and finally cubes on supports. We rejected results from single melt tracks due to poor consistency and reproducability, probably resulting from the flexible recoater lip made of silicone rubber being used. The results of thin walls, cubes and cubes on supports confirmed that process windows can qualitatively be estimated and compared between different alloys already from thin walls. These can be build up much quicker and evaluated with less effort than cube samples. For cubes on supports we achieved higher relative densities than for cubes on platforms. A reason may be the heat abduction from the melt pool, which should be slowed down by the smaller cross section area of thin-wall-supports and the insulating loose powder in between them. Higher absolute laser power than the used 100°W might result in an LBM process less susceptible to disturbances. On the other hand, larger parts with more complex geometries than the investigated cubic samples of 5 mm edge length might lead to larger variations in heat abduction.

Further investigations which we have already begun are mechanical characterization by tensile and compressive tests of samples in heat treated and as-built state, as well as fully comparative studies with cubes on supports built from the state-of-the-art alloy AC-43000, also known as AlSi10Mg.

Acknowledgments

References

[1]   Buchbinder, D.: Generative Fertigung von Aluminiumbauteilen für die Serienproduktion. AluGenerativ Abschlussbericht BMBF 01RIO639A-D, 2010

[2]   http://asm.matweb.com/search/SpecificMaterial.asp?bassnum=MA2024T4,   accessed October 2013

[3]   Ihno Beek: Werkstoffkundliche Aspekte des Schweißens aushärtbarer Aluminiumlegierungen mit gepulsten Festkörperlasern. Dissertation, TU Clausthal, 1996.

[4]   U. Dilthey: Schweißtechnische Fertigungsverfahren 2. Schweißen von Aluminiumwerkstoffen, 3. Auflage. Berlin: Springer-Verlag, 2005.

[5]   Hesse, W.: Aluminium-Schlüssel, Berlin: Beuth Verlag, 2012.

[6]   Aluminium Association, International Alloy Designations and Chemical Composition Limits for Wrought Aluminum and Wrought Aluminum Alloys, 2009

[7]   DIN EN 1706:2013-12 Aluminium und Aluminiumlegierungen - Gussstücke - Chemische Zusammensetzung und mechanische Eigenschaften; EN 1706:2010

[8]   DIN EN 573-3:2013-12 Aluminium und Aluminiumlegierungen - Chemische Zusammensetzung und Form von Halbzeug - Teil 3: Chemische Zusammensetzung und Erzeugnisformen, EN 573-3:2013

[9]   Drahtwerk Elisental W. Erdmann GmbH & Co: Elisental Schweißzusätze Hauptprospekt. URL: http://www.elisental.de/pdf_de/Schweisszusaetze_Hauptprospekt.pdf. Accessed October 2013.

[10]   H. Herold: Rissminderung beim Schweißen von Al-Legierungen mittlerer und höherer Festigkeit. Schlussbericht für den Zeitraum 1.02.2005-31.01.07, AiF-Vorhaben Nr. 13. 983B, Magdeburg, 2007

[11]   DIN EN ISO 18273 Schweißzusätze - Massivdrähte und -stäbe zum Schmelzschweißen von Aluminium und Aluminiumlegierungen, 2004

[12]   H. Schoer: Schweißen und Hartlöten von Aluminiumwerkstoffen. Düsseldorf: DVS-Verlag, 2002

[13]   DIN EN ISO 14174 Schweißzusätze - Pulver zum Unterpulverschweißen und Elektroschlackeschweißen - Einteilung (2012).

[14]   Profi Schweißen Internetseite. URL: http://www.profi-schweissen.de/schweissen/wolfram-inertgasschweissen-schweisszusatz-individuell/. Accessed November 2013.

[15]   http://www.dvs-ma-lu.de/Downloads/Aluminium-Schweissen.pdf. Accessed October 2012

[16]   G. Schulze: Die Metallurgie des Schweißens. 3rd Edition, Springer, 2004

[17]   General Electric Company: World's First Plant to Print Jet Engine Nozzles in Mass Production. Press Release July 15th 2014 http://www.gereports.com/post/91763815095/worlds-first-plant-to-print-jet-engine-nozzles-in-mass accessed August 28th 2014

[18]   http://asm.matweb.com/search/SpecificMaterial.asp?bassnum=MA2024T3 Accessed August 2014

[19]   E. Hornbogen: Hundred years of precipitation hardening. Journal of Light Metals, 2001 Science) 1 (2): 127–132. doi:10.1016/S1471-5317(01)00006-2